

Rejecting proposed dense-matter equations of state with quiescent low-mass X-ray binaries

Sebastien Guillot and Robert E. Rutledge

*Department of Physics, McGill University,
3600 rue University, Montreal, QC, Canada, H3A-2T8*

guillots@physics.mcgill.ca, rutledge@physics.mcgill.ca

ABSTRACT

Neutron stars are unique laboratories for discriminating between the various proposed equations of state of matter at and above nuclear density. One sub-class of neutron stars – those inside quiescent low-mass X-ray binaries (qLMXBs) – produce a thermal surface emission from which the neutron star radius (R_{NS}) can be measured, using the widely accepted observational scenario for qLMXBs, assuming unmagnetized H atmospheres. In a combined spectral analysis, this work first reproduces a previously published measurement of the R_{NS} , assumed to be the same for all neutron stars, using a slightly expanded data set. The radius measured is $R_{\text{NS}} = 9.4 \pm 1.2$ km. On the basis of spectral analysis alone, this measured value is not affected by imposing an assumption of causality in the core. However, the assumptions underlying this R_{NS} measurement would be falsified by the observation of any neutron star with a mass $> 2.6 M_{\odot}$, since radii < 11 km would be rejected if causality is assumed, which would exclude most of the R_{NS} parameter space obtained in this analysis. Finally, this work directly tests a selection of dense matter equations of states: WFF1, AP4, MPA1, PAL1, MS0, and three versions of equations of state produced through chiral effective theory. Two of those, MS0 and PAL1, are rejected at the 99% confidence level, accounting for all quantifiable uncertainties, while the other cannot be excluded at $>99\%$ certainty.

1. Introduction

More than eighty years after the discovery of the neutron, much uncertainty surrounds theoretical predictions related to strong-force physics. One prediction, the dense matter equation of state (dEOS hereafter) relates the pressure and density of cold matter at and above nuclear density $\rho_0 \gtrsim 10^{14}$ g cm $^{-3}$, such as that found in the core of neutron stars (NSs). The dEOS is still actively debated among nuclear physicists (Lattimer & Prakash 2007), with dEOS theories proposed based upon a variety of uncertain physical processes and calculational methods (Müther et al. 1987; Wiringa et al. 1988; Prakash et al. 1988; Müller & Serot 1996; Akmal & Pandharipande 1997; Hebeler et al. 2013). Because knowledge of

the masses and radii of NSs permit discrimination between dEOSs, these compact objects have been extensively observed (e.g., Lindblom 1992; Özel & Psaltis 2009; Guillot et al. 2013, G13 hereafter).

One sub-class of NSs – those inside quiescent low-mass X-ray binaries (qLMXBs) – produce thermal surface emission from which constraints on the NS mass M_{NS} and radius R_{NS} can be extracted (Brown et al. 1998; Rutledge et al. 1999). In this widely invoked model, the luminosity originates from energy deposited in the NS crust during active accretion ($E \sim 1.9$ MeV per accreted nucleon Haensel & Zdunik 2008), by a series of electron captures, neutron emissions and pycnonuclear reactions. Once an active accretion episode ends, this heat, mostly absorbed into the rela-

tively cool core, is then conducted to the surface on a core-cooling timescale, before being radiated through the NS atmosphere (Brown et al. 1998).

Hydrogen atmosphere models for these NSs (Rajagopal & Romani 1996; Zavlin et al. 1996; McClintock et al. 2004; Heinke et al. 2006; Haakonsen et al. 2012) consider the full radiative transfer through an accreted hydrogen atmosphere of an unmagnetized NS, including the gravitational redshift $1 + z = \left(1 - \frac{2GM_{\text{NS}}}{R_{\text{NS}}c^2}\right)^{-1/2}$ caused by the high surface gravity $\sim 10^{13} - 10^{15} \text{ cm s}^{-2}$. These models describe well the emergent spectra of qLMXBs and the measured emission areas correspond to the $\sim 10 \text{ km}$ radii expected from NSs. This scenario has been found to be consistent with behavior in multiple historical transient LMXBs in their quiescent phase (e.g. Rutledge et al. 1999, 2000; Campana et al. 2000; in't Zand et al. 2001; Rutledge et al. 2001b,a; Wijnands et al. 2002; Tomsick et al. 2004; Cackett et al. 2006; Jonker et al. 2007; Cornelisse et al. 2007; Fridriksson et al. 2010; Degenaar et al. 2014).

While the higher signal-to-noise ratio (S/N) X-ray spectra of qLMXBs in the field of the galaxy (e.g., Cen X-4, Aql X-1) can potentially place useful constraints on the dEOS from the measurement of the projected radius $R_{\infty} = R_{\text{NS}}(1 + z)$, the 20–50% distance uncertainty to these sources directly contributes to a 20–50% uncertainty of the R_{∞} measurements. Focusing on qLMXBs located inside globular clusters (GCs), for which distances are known to ~ 5 –10% accuracy, decreases the associated uncertainty, and so targets identified as qLMXBs in GCs are exclusively used for this analysis.

Because of their relatively low-S/N – but more importantly because of the strong covariance between M_{NS} and R_{NS} in this spectral interpretation – the X-ray spectra of qLMXBs inside GCs have individually been hitherto unable to place stringent constraints on the dEOS (Webb & Barret 2007; Heinke et al. 2006). Combining these X-ray spectra in a single, simultaneous analysis increases the S/N; more significantly, comparing an ensemble of $M_{\text{NS}}-R_{\text{NS}}$ constraints directly to a single proposed $M_{\text{NS}}(R_{\text{NS}})$ relation resulting from a theoretical dEOS produces strong covariance between photon spectral model parameters in different sources.

This results in a stronger confrontation between theory and data than obtained when treating sources independently. This was done in a previous work to measure the radius of NSs, $R_{\text{NS}} = 9.1_{-1.5}^{+1.3} \text{ km}$ (90% confidence, G13), using five qLMXBs located in GCs, when it is assumed that these NSs have a quasi-constant R_{NS} ($\text{Cst}R_{\text{NS}}$, hereafter), i.e., the same value of R_{NS} to within measurement uncertainties. This assumption arises from the observational evidence (M_{NS} measurements of two $\sim 2 M_{\odot}$ pulsars, Demorest et al. 2010; Antoniadis et al. 2013) that dense nuclear matter is best described by dEOSs characterized by a quasi-constant R_{NS} for astrophysically relevant masses ($M_{\text{NS}} > 0.5 M_{\odot}$).

Significantly, an analysis (Steiner et al. 2013) employing qLMXB spectral parameters (Heinke et al. 2006; Webb & Barret 2007; Guillot et al. 2011) separately, and in combination with photospheric radius expansion analysis spectral parameters (Özel et al. 2009; Güver et al. 2010a,b; Özel et al. 2012) derived a detailed formulation for the dEOS. By assuming the dEOS would be consistent with producing a measured $\sim 2 M_{\odot}$ NS (Demorest et al. 2010), it was found that the preferred NS $M_{\text{NS}}-R_{\text{NS}}$ relationship produces quasi-constant NS radii, demonstrating consistency with this assumption (Steiner et al. 2013). Furthermore, this work showed that the radius of a $1.4 M_{\odot}$ NS is contained within 11.23 km and 12.49 km (95% confidence region), which, according to that work, rules out $\sim 1/3$ of Skyrme models as well as covariant field-theoretical dEOS models, although without stating the quantified probability with which these dEOS models are ruled out.

Here, widely used observational analyses are employed, but with a new statistical analysis combining the data from six qLMXBs, comparing them directly to $M_{\text{NS}}(R_{\text{NS}})$ relationships resulting from proposed dEOSs. This method permits rejecting dEOSs with a quantifiable degree of certainty. Section 2 summarizes the spectral analysis, also available in greater detail in a previous work (G13), and presents the additional data added to this work. Section 3 reproduces the results of the previous work with the additional data, and adding the assumption of causality. Section 4 describes the analysis confronting a selection of dEOS models to the spectral X-ray data. Finally, Section 5 discusses these results.

TABLE 1
RADIUS MEASUREMENTS OF NEUTRON STARS

Description of Simulation	R_{NS} (km) 90% confidence	R_{NS} (km) 99% confidence	χ^2 / d.o.f.	Null Hypothesis Probability	Line style in Figure 1 (<i>top</i>)
Causality assumption	$9.5^{+1.2}_{-1.2}$	$9.5^{+1.9}_{-1.8}$	516 / 476	0.10	Solid
No causality assumption	$9.4^{+1.2}_{-1.2}$	$9.4^{+1.6}_{-1.8}$	516 / 476	0.10	Dashed
Guillot et al. (2013)	$9.1^{+1.3}_{-1.5}$	$9.1^{+2.0}_{-2.2}$	613 / 628	0.64	Dotted

NOTE.—No significant variation of the measured R_{NS} is observed, when additional data are added (for qLMXBs in M30 and ω Cen) to the spectra used in the previous work (G13). Assuming causality does not change R_{NS} by more than 1%. For the analysis with the causality assumption, MCMC samples violating the condition $R_{\text{NS}} < 2.83GM_{\text{NS}}/c^2$ are excluded.

2. Simultaneous spectral fitting of qLMXBs with H-atmosphere models

The simultaneous spectral analysis of the qLMXBs is performed using the Markov Chain Monte Carlo (MCMC) described in a previous work (G13). The spectral model used is the NS hydrogen atmosphere model `nsatmos` (Heinke et al. 2006) modulated by galactic absorption modeled with `wabs` (Morrison & McCammon 1983). In all runs, convergence is ensured by visual inspection of the parameters traces, and with the Geweke test (Geweke 1992).

The previous work accounted for and quantified the dominant sources of uncertainties, and presented a detailed description of the analysis assumptions possibly affecting the results (G13). These assumptions, also used in the present work, include: (1) isotropic NS surface thermal emission through (2) an un-magnetized ($B \lesssim 10^9$ G) and (3) H atmosphere of (4) non-rotating NSs.

Others (Lattimer & Steiner 2014) have extrapolated the previous $M_{\text{NS}}-R_{\text{NS}}$ constraints from qLMXBs (G13) under an altered assumption of He-atmosphere – rather than H atmosphere – unmagnetized transient NSs with thermal spectra in quiescence, such as have been predicted (Bildsten & Deloye 2004; Ivanova et al. 2008), obtaining a different R_{NS} value. However, to date, no such objects have been observed (Lattimer & Steiner 2014). In contrast, a literature search finds at least several H-companion, unmagnetized, transient LMXBs which have had thermal emission detected in quiescence (e.g., Cen X-4, Aql X-1, 4U 1608-522, MXB 1659-29, XTE J2123-058).

The present work assumes that all of the qLMXB targets have unmagnetized H atmospheres. While it is not observationally demonstrated that all of these targets are H atmosphere, and not He atmosphere, one (ω Cen) is observed with $H\alpha$ disk emission, indicating a H-companion, and so a H atmosphere NS (Haggard et al. 2004).

Under the forgoing assumptions, the `nsatmos` photon spectral emission model is fit to data from each qLMXB, with 5 model parameters for each source (i) consisting of: (1) the distance to each source; (2) an effective surface temperature; (3) an equivalent hydrogen column density, accounting for line-of-sight absorption between the observer and the source; (4) a NS mass $M_{\text{NS},i}$; and (5) a normalization for a power-law spectral component (unrelated to the surface emission) with an assumed photon spectral slope of 1. The final parameter, R_{NS} , is alternatively an independent, free parameter common to all NSs in the `Cst` R_{NS} model; or is dependent on $M_{\text{NS},i}$ when dEOS models are imposed.

The distances to each NS are included using Gaussian Bayesian prior distributions derived from previous GC distance measurements: for the NSs used in the previous work, the same distance priors are used (G13); for M30, $d_{\text{M30}} = 9.0 \pm 0.5$ kpc (Carretta et al. 2000; Lugger et al. 2007).

3. Constant R_{NS} analysis

In this Letter, the same qLMXBs as the previous work are included in the sample (G13): the qLMXBs in the GCs M28, NGC 6397, M13, ω Cen, and NGC 6304, observed with the *Chandra X-*

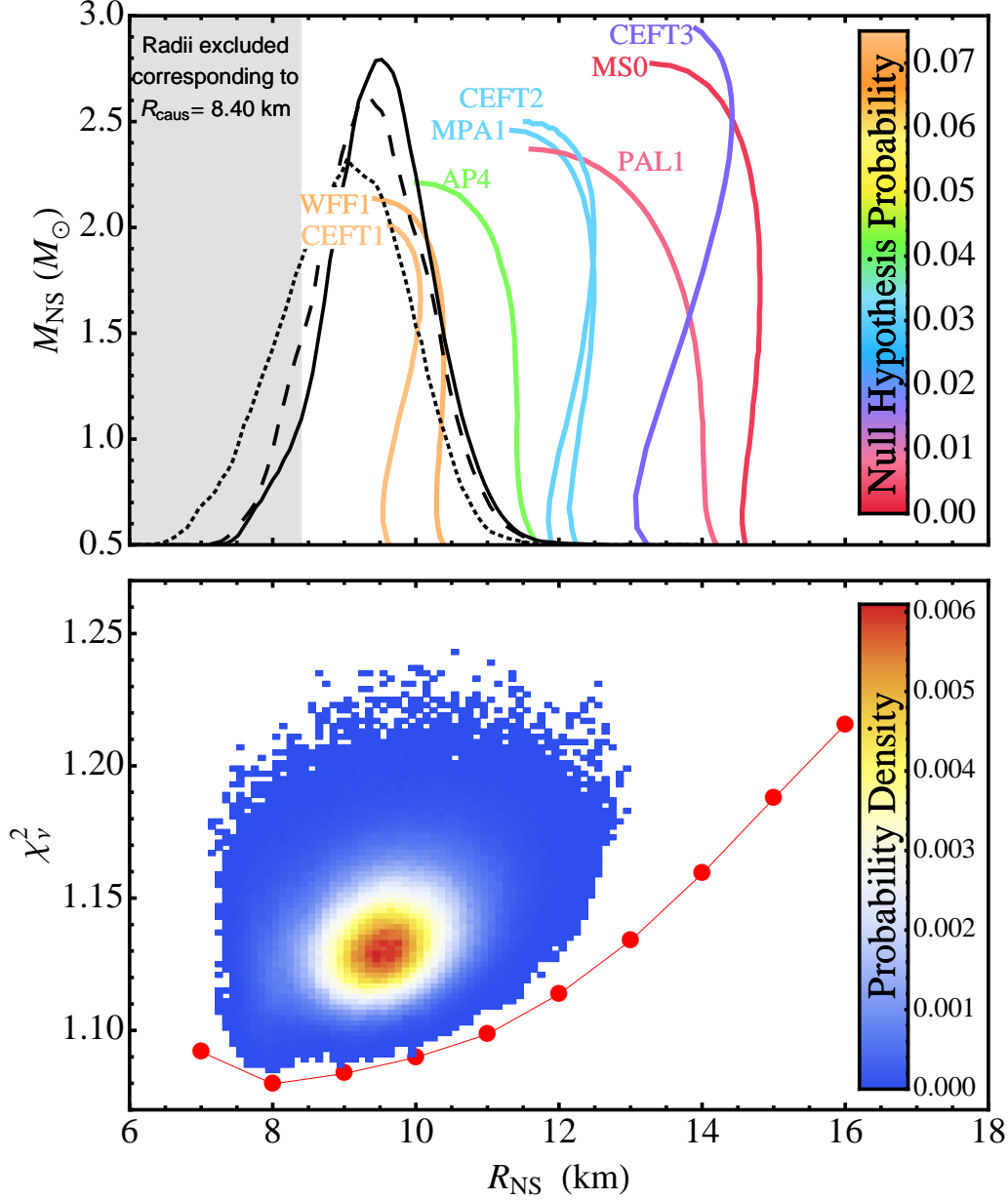


Fig. 1.— (top) In black, the normalized posterior PDFs of R_{NS} are shown, in the three cases of the $\text{Cst}R_{\text{NS}}$ assumption listed in Table 1: considering causality (solid black curve), without considering causality (dashed black curve), and the R_{NS} PDF of the previous work (G13), respectively. The M_{NS} axis does not apply to these PDFs. The gray area represents radii excluded by $R_{\text{caus}} < 2.83GM_{\text{NS}}/c^2$, resulting from the existence of a $2.01 M_{\odot}$ NS respecting causality. The tested dEOSs in $M_{\text{NS}}-R_{\text{NS}}$ space are color-coded by null hypothesis probabilities (NHPs, right color bar). PAL1 and MS0 are rejected with 99% confidence, since their NHPs are smaller than 0.01. (bottom) Best reduced χ^2_v obtained when fixing R_{NS} to the values in red (from 7 km to 17 km), and 2D distribution of the χ^2_v for accepted radius values in the MCMC run with the $\text{Cst}R_{\text{NS}}$ assumption.

ray Observatory ACIS-S/I detectors or with the *XMM-Newton* pn camera. To these, the spectrum of the qLMXB in M30 observed with *Chandra* (ObsID 2679, Lugger et al. 2007) and 200 ks of recently archived *Chandra* observations of the qLMXB in the GC ω Cen (ObsIDs 13726 and 13727) are added. These added spectral data increase the S/N by 7% compared to the previous analysis (G13). Data processing and analysis follow the standard procedures, previously used and described in detail (G13). However, *Chandra* and *XMM* data have been re-processed with CIAO v4.5 (with CALDB v4.5.5, Graessle et al. 2007) and XMMSAS v12.0.

For ω Cen, the addition of ~ 200 ks of spectral data improves the constraints on R_∞ and N_H , when analyzed alone. Specifically, $R_\infty = 13.5^{+4.2}_{-3.0}$ km at $d = 4.8$ kpc, using all the available data, compared to $R_\infty = 23.6^{+7.6}_{-7.1}$ km at $d = 4.8$ kpc using the *XMM* and 2000 *Chandra* data in G13. A recent publication (Heinke et al. 2014) also reports this large difference in the measured radius: $R_{\text{NS}} = 20.3^{+9.1}_{-6.7}$ km at $1.4 M_\odot$ with the same data as G13, and $R_{\text{NS}} = 11.5^{+3.4}_{-3.5}$ km at $1.4 M_\odot$ when all available data are used, both assuming $d = 5.3$ kpc, and with the `wabs` absorption model. Using the $d = 5.3$ kpc, we find that the physical radius at $1.4 M_\odot$ is $R_{\text{NS}} = 11.7^{+3.6}_{-5.3}$ km, consistent with that of Heinke et al. (2014). Furthermore, the choice of absorption model does not significantly change the radius measured. The R_{NS} are consistent with the measured R_{NS} of Heinke et al. (2014) whether the `wabs` or `wilms` ($R_{\text{NS}} = 10.0^{+2.6}_{-5.0}$ km) models are used.

Using these X-ray data in the MCMC analysis framework, the $\text{Cst}R_{\text{NS}}$ analysis of the previous work (G13) is first reproduced. An additional analysis is performed for comparison purposes. It employs the assumption of causality, imposing that the speed of sound in the NS core should not exceed the speed of light, i.e., $dP/d\rho \leq c^2$. This assumption produces a NS radius $R_{\text{caus}} = 2.83GM_{\text{NS}}/c^2$ above which, the NS would be unstable against collapse (Lattimer & Prakash 2007). Thus, “imposing causality” in this analysis means that MCMC trials in which $R_{\text{NS}} < 2.83GM_{\text{NS},i}/c^2$ are summarily rejected.

It is found that the R_{NS} posterior probability distribution function (PDF) measured with or without the assumption of causality are consis-

tent with each other and with that of the previous work (G13). These results are shown in Table 1 and Figure 1 (top panel, black lines). With 90% confidence, the resulting NS radius is $R_{\text{NS}} = 9.4 \pm 1.2$ km. When causality is imposed, $R_{\text{NS}} = 9.5 \pm 1.2$ km¹. Figure 2 shows the posterior distributions in $M_{\text{NS}}-R_{\text{NS}}$ space resulting from the $\text{Cst}R_{\text{NS}}$ toy model run (without and with the causality assumption, respectively), and the hard priors imposed in this analysis.

Note, importantly, that imposing the causality constraint does not shift the $\text{Cst}R_{\text{NS}}$ posterior PDF to higher radii (Figure 2), but simply rejects parts of the $M_{\text{NS}}-R_{\text{NS}}$ parameter $M_{\text{NS}}-R_{\text{NS}}$ space. The existence of large-mass NSs (Demorest et al. 2010; Antoniadis et al. 2013) combined with the causality condition leads to a minimum acceptable value of R_{NS} . In other words, the effect of larger mass NSs being detected is to exclude the part of the $\text{Cst}R_{\text{NS}}$ posterior PDF below the corresponding R_{caus} . For example, for $M_{\text{NS}} = 2.01 M_\odot$, $R_{\text{caus}} = 8.40$ km excludes R_{NS} parameter space below this value (see Figure 1). As a consequence, there is significant tension between the $\text{Cst}R_{\text{NS}}$ result and high-mass NSs. Therefore, a definitive measurement of a $2.6 M_\odot$ NS – within the uncertainty of a $2.40 \pm 0.12 M_\odot$ pulsar (van Kerkwijk et al. 2011) – would rule out a $\text{Cst}R_{\text{NS}}$ radius < 11.0 km, essentially all the R_{NS} acceptable parameter space obtained here. This would falsify the conclusions of this work, and therefore one or more of the assumptions made.

4. Testing proposed dEOSs

Here, it is measured to what degree of certainty a selection of popular proposed dEOSs fit the spectra of the six qLMXBs in the sample. This spectral analysis is performed with the MCMC analysis described above by forcing the fitted M_{NS} and R_{NS} parameters to be constrained to the $M_{\text{NS}}(R_{\text{NS}})$ curve of a user-defined dEOS. To do so, the MCMC-sampled parameters are not the M_{NS} and R_{NS} of each NSs, but instead a parameter between 0 and 1 representing the position on the dEOS curve, with 0 at the tip (at M_{max}), and 1 at the $M_{\text{NS}} = 0.5 M_\odot$ point (see posterior PDFs in Figure 3).

¹It should not be necessary to impose the causality assumption in this analysis as, surely, nature imposes it for us.

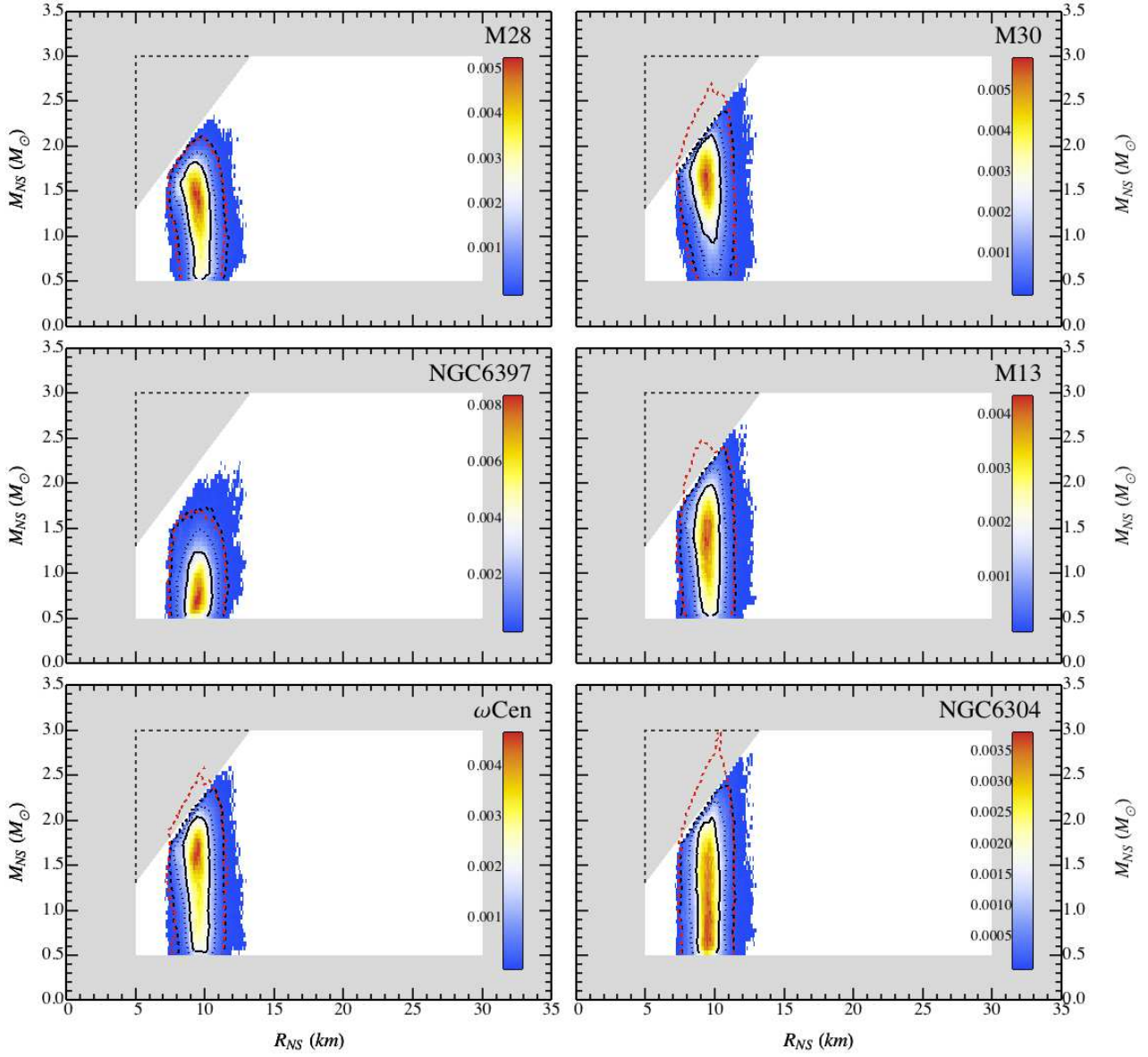


Fig. 2.— Figure showing the posterior distributions in $M_{\text{NS}}-R_{\text{NS}}$ space for the Cst R_{NS} toy model. The gray-shaded areas show the priors on M_{NS} and R_{NS} (hard limits of `nsatmos`, dashed straight lines), to which the causality-imposed exclusion region is added ($R_{\text{NS}} < 2.83GM_{\text{NS},i}/c^2$). Black solid, Dotted and Dashed contours correspond to the 68%, 90% and 99% enclosures. The red contour is the 99% enclosure obtained without the causality assumption.

TABLE 2
STATISTICAL REJECTION OF DENSE MATTER EQUATIONS OF STATE

Equation of State	Reference	χ^2 / dof	Null Hypothesis Probability	Acceptance Rate %
WFF1	Wiringa et al. (1988)	523 / 477	0.073	6.6%
AP4	Akmal & Pandharipande (1997)	531 / 477	0.044	7.2%
MPA1	Müther et al. (1987)	536 / 477	0.031	7.5%
PAL1	Prakash et al. (1988)	557 / 477	0.007	8.5%
MS0	Müller & Serot (1996)	565 / 477	0.003	8.2%
CEFT1	Hebeler et al. (2013)	520 / 477	0.084	6.5%
CEFT2	Hebeler et al. (2013)	536 / 477	0.031	7.3%
CEFT3	Hebeler et al. (2013)	547 / 477	0.014	7.8%

NOTE.—The dEOS are ordered by increasing average radius. The χ^2 -statistics listed is the resulting minimum χ^2 obtained from the MCMC analysis described in the text.

To determine which dEOS is quantitatively preferred by the data, five dEOSs with varied stiffness are tested, as well as three representative dEOSs obtained from chiral effective field theory (Hebeler et al. 2013): the Soft, Intermediate and Stiff representative dEOSs (labeled CEFT1, CEFT2, and CEFT3 here). For each dEOS, the minimum χ^2 and the corresponding null hypothesis probability (NHP) are obtained after convergence of the MCMC simulation. The NHP is the probability of finding by chance a χ^2 as large or larger as the minimum χ^2 found if the model is correct. Results are shown in Table 2 and Figure 1. The MCMC runs testing the eight dEOSs have acceptance rates in the range $\sim 6 - 9\%$. In addition, one can notice that the NHP decreases as the average radius, i.e. the stiffness, of the tested dEOS, increases.

To the reader, there may appear to be a discrepancy between the NHPs obtained when testing dEOSs and the likelihood distributions of the Cst R_{NS} case (Figure 1, *top*). Specifically, on the one hand, the posterior PDFs of R_{NS} indicates that $R_{\text{NS}} = 14$ km is $\sim 6\sigma$ away from the median of the distribution. On the other hand, the test for MS0 (with average radius ~ 14 km) gives a NHP of 0.003, i.e., MS0 is rejected at the 99.7% confidence ($\sim 3\sigma$).

This is better illustrated with Figure 1 (*bottom*) showing the 2D distribution of the χ^2_ν value as a function of R_{NS} for all accepted MCMC steps of the Cst R_{NS} analysis (no causality assumed), revealing the extent of the radius coverage. The

plot also shows the minimum χ^2_ν (red) obtained when the R_{NS} is fixed to a selection of values (7–16 km), essentially a selection of toy model dEOSs. The minimum χ^2_ν of the 2D distribution follows the minimum χ^2_ν of the red line in the range 7–11 km, but becomes systematically larger above 12 km and disappears above 13 km. This apparent difference (between the Bayesian-accepted parameter space and the minimum χ^2_ν values at each R_{NS}) is similar to the difference between confidence levels described in the previous paragraph. This emerges as a consequence of the complicated parameter space above 12 km in the Cst R_{NS} run; the probability of excursion to radii larger than 12 km during the MCMC run is low since such steps are more likely to be rejected, making it difficult for the MCMC to populate this area of the parameter space.

This justification is investigated with the rejected MCMC steps in the Cst R_{NS} analysis. As the R_{NS} goes to larger values, the NS masses are forced to smaller values to maintain the R_∞ values that fits the spectral data of each NS. A constant $R_\infty = R_{\text{NS}} (1 - 2GM_{\text{NS}}/R_{\text{NS}}c^2)^{-1/2}$ implies for large R_{NS} , smaller M_{NS} . As a result, an increasing proportion of MCMC steps are rejected because the mass parameters are more likely to lie outside the allowed range of values ($0.5-3.0 M_\odot$, the hard limits of the `nsatmos` model). A significant fraction (93.2%) of the proposed steps with $R_{\text{NS}} > 13$ km are rejected simply due to one or more $M_{\text{NS},i}$ being outside the prior limits. For comparison, when all radii are considered, only

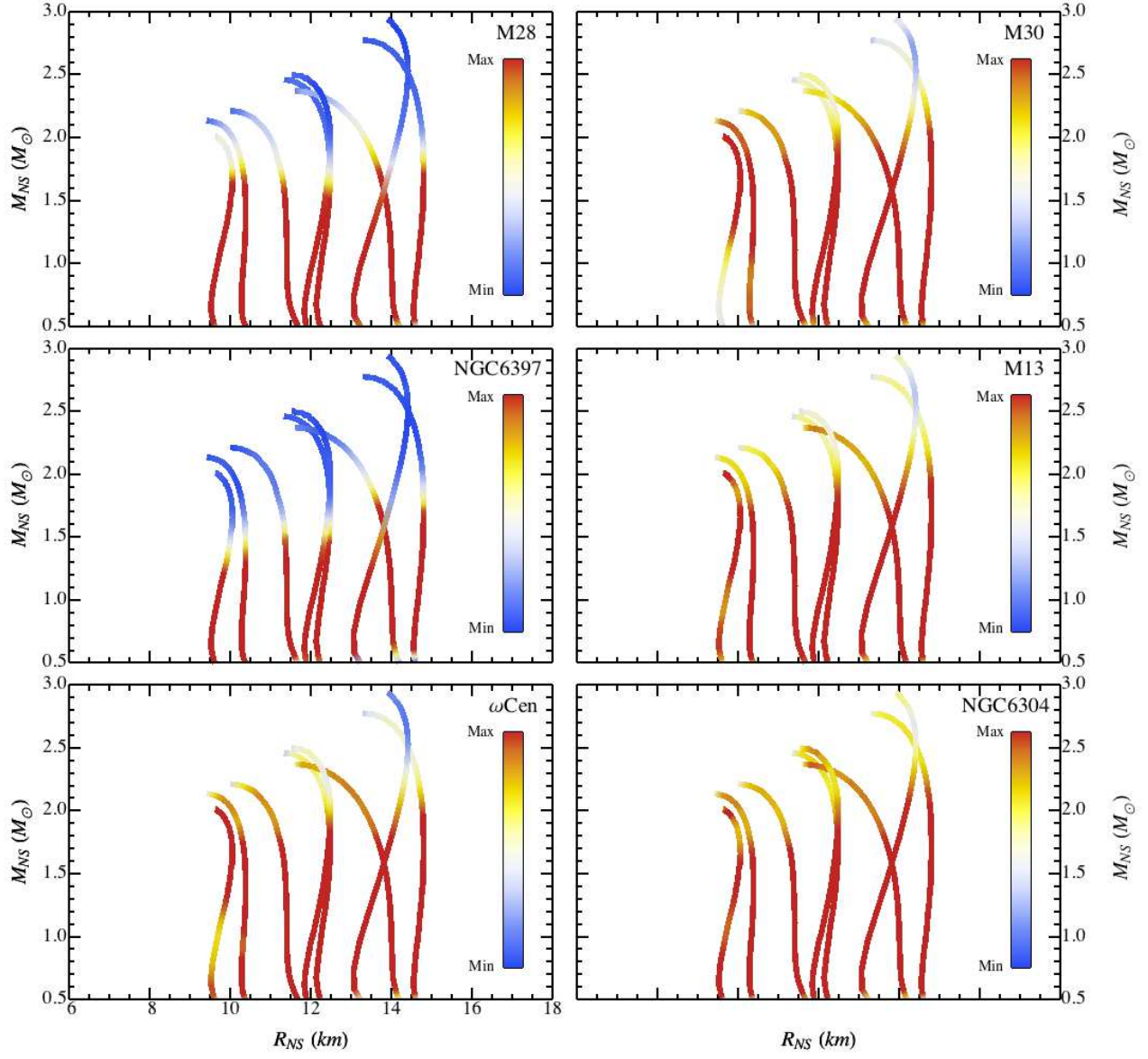


Fig. 3.— Figure showing the posterior distributions in M_{NS} – R_{NS} space for all the tested dEOSs. Each curve is colored by the value of the PDFs (different for each dEOSs, therefore the color bar only shows “Min” and “Max”). In the MCMC runs testing dEOS models, the M_{NS} and R_{NS} are constrained to remain on the dEOS with the use of a position parameter sampling the $M_{NS}(R_{NS})$ curve between $0.5M_{\odot}$ and M_{\max} . Therefore, the priors for M_{NS} and R_{NS} are the $M_{NS}(R_{NS})$ curves of the dEOSs.

40.4% of proposed steps are rejected due to one or more $M_{\text{NS},i}$ being outside the hard limits. Interestingly, we note that a larger minimum M_{NS} value (assumed from theory) would result in an even lower maximum radius from this Bayesian analysis.

To further test that the observation illustrated in Figure 1 (*bottom*) is a consequence of the shape of the parameter space, a separate $\text{Cst}R_{\text{NS}}$ trial is performed, in which all MCMC walkers were initiated with $R_{\text{NS}} > 13$ km. The walkers are all observed to “move” and converge into the final parameter space of Figure 1 (*bottom*), with all $R_{\text{NS}} < 13$ km, as expected from the MCMC algorithm.

The “noisy” parameter space occurs because of the strong covariance between the 32 model parameters in the $\text{Cst}R_{\text{NS}}$ analysis. Overall, the apparent difference between the acceptable parameter space from the MCMC analysis and the χ^2 analysis is due to the fact that Bayesian and χ^2 statistics rely on different assumptions about the statistical system. This underscores the need for a Monte Carlo integration to assess most-likely parameters and uncertainty regions, rather than relying upon the χ^2 curvature matrix.

Overall, this minimum χ^2 values obtained for each dEOS tested in this analysis, and their corresponding NHPs, provide a quantitative confrontation between the proposed physical models and the X-ray spectral data of qLMXBs.

5. Conclusion

This work first updated the $\text{Cst}R_{\text{NS}}$ measurement presented in a previous work (G13), including additional spectral data (for the qLMXBs in ω Cen and M13), and finding $R_{\text{NS}} = 9.4 \pm 1.2$ km (90% confidence), consistent with the previous work. It was found that the inclusion of causality does not significantly affect the posterior PDFs in the $\text{Cst}R_{\text{NS}}$ toy model.

In the second part of this work, the simultaneous spectral analysis was performed by constraining the M_{NS} and R_{NS} parameters of the six qLMXBs on the $M_{\text{NS}}(R_{\text{NS}})$ relations of a selection of tested EOSs. The resulting statistics from the MCMC spectral fitting permits rejection of the dEOSs PAL1 and MS0 on the basis of the NHPs obtained, 0.007 and 0.003, respectively.

In conclusion, two of the dEOSs tested (PAL1, Prakash et al. 1988 and MS0, Müller & Serot 1996) have $\text{NHP} < 0.01$, rejecting these theoretical dEOSs as adequate descriptions of the behavior of cold nuclear matter with $>99\%$ confidence, under the assumptions of this work. This is the first time that a selection of proposed dEOSs are conservatively excluded with quantitative probabilities of consistency, using an analysis of qLMXB X-ray Spectra.

Acknowledgements S.G. and R.E.R acknowledge the support of NSERC via the Vanier CGS and Discovery grant programs. The authors acknowledge useful and enlightening conversation with David W. Hogg on MCMC particulars.

REFERENCES

- Akmal, A. & Pandharipande, V. R. 1997, Phys. Rev. C, 56, 2261
- Antoniadis, J. et al. 2013, Science, 340, 448
- Bildsten, L. & Deloye, C. J. 2004, ApJ, 607, L119
- Brown, E. F., Bildsten, L., & Rutledge, R. E. 1998, ApJ, 504, L95+
- Cackett, E. M., Wijnands, R., Linares, M., Miller, J. M., Homan, J., & Lewin, W. H. G. 2006, MNRAS, 372, 479
- Campana, S., Stella, L., Mereghetti, S., & Cremonesi, D. 2000, A&A, 358, 583
- Carretta, E., Gratton, R. G., Clementini, G., & Fusi Pecci, F. 2000, ApJ, 533, 215
- Cornelisse, R., Wijnands, R., & Homan, J. 2007, MNRAS, 380, 1637
- Degenaar, N., Wijnands, R., & Miller, J. M. 2014, ApJ, 787, 67
- Demorest, P. B., Pennucci, T., Ransom, S. M., Roberts, M. S. E., & Hessels, J. W. T. 2010, Nature, 467, 1081
- Fridriksson, J. K. et al. 2010, ApJ, 714, 270
- Geweke, J. 1992, in Bayesian Statistics, ed. J. M. Bernardo, J. O. Berger, A. P. Dawid, & A. F. M. Smith, Vol. 4 (Oxford, UK: Clarendon Press)

- Graessle, D. E., Evans, I. N., Glotfelty, K., He, X. H., Evans, J. D., Rots, A. H., Fabbiano, G., & Brissenden, R. J. 2007, *Chandra News*, 14, 33
- Guillot, S., Rutledge, R. E., & Brown, E. F. 2011, *ApJ*, 732, 88
- Guillot, S., Servillat, M., Webb, N. A., & Rutledge, R. E. 2013, *ApJ*, 772, 7
- Güver, T., Özel, F., Cabrera-Lavers, A., & Wroblewski, P. 2010a, *ApJ*, 712, 964
- Güver, T., Wroblewski, P., Camarota, L., & Özel, F. 2010b, *ApJ*, 719, 1807
- Haakonsen, C. B., Turner, M. L., Tacik, N. A., & Rutledge, R. E. 2012, *ApJ*, 749, 52
- Haensel, P. & Zdunik, J. L. 2008, *A&A*, 480, 459
- Haggard, D., Cool, A. M., Anderson, J., Edmonds, P. D., Callanan, P. J., Heinke, C. O., Grindlay, J. E., & Bailyn, C. D. 2004, *ApJ*, 613, 512
- Hebeler, K., Lattimer, J. M., Pethick, C. J., & Schwenk, A. 2013, *ApJ*, 773, 11
- Heinke, C. O. et al. 2014, *MNRAS*, 444, 443
- Heinke, C. O., Rybicki, G. B., Narayan, R., & Grindlay, J. E. 2006, *ApJ*, 644, 1090
- in't Zand, J. J. M., van Kerkwijk, M. H., Pooley, D., Verbunt, F., Wijnands, R., & Lewin, W. H. G. 2001, *ApJ*, 563, L41
- Ivanova, N., Heinke, C. O., Rasio, F. A., Belczynski, K., & Fregeau, J. M. 2008, *MNRAS*, 386, 553
- Jonker, P. G., Bassa, C. G., & Wachter, S. 2007, *MNRAS*, 377, 1295
- Lattimer, J. M. & Prakash, M. 2007, *Phys. Rep.*, 442, 109
- Lattimer, J. M. & Steiner, A. W. 2014, *ApJ*, 784, 123
- Lindblom, L. 1992, *ApJ*, 398, 569
- Lugger, P. M., Cohn, H. N., Heinke, C. O., Grindlay, J. E., & Edmonds, P. D. 2007, *ApJ*, 657, 286
- McClintock, J. E., Narayan, R., & Rybicki, G. B. 2004, *ApJ*, 615, 402
- Morrison, R. & McCammon, D. 1983, *ApJ*, 270, 119
- Müller, H. & Serot, B. D. 1996, *Nuclear Physics A*, 606, 508
- Müther, H., Prakash, M., & Ainsworth, T. L. 1987, *Physics Letters B*, 199, 469
- Özel, F., Güver, T., & Psaltis, D. 2009, *ApJ*, 693, 1775
- Özel, F. & Psaltis, D. 2009, *ArXiv e-prints*
- Özel, F., Psaltis, D., Narayan, R., & Santos Villarreal, A. 2012, *ApJ*, 757, 55
- Prakash, M., Lattimer, J. M., & Ainsworth, T. L. 1988, *Physical Review Letters*, 61, 2518
- Rajagopal, M. & Romani, R. W. 1996, *ApJ*, 461, 327
- Rutledge, R. E., Bildsten, L., Brown, E. F., Pavlov, G. G., & Zavlin, V. E. 1999, *ApJ*, 514, 945
- 2000, *ApJ*, 529, 985
- 2001a, *ApJ*, 559, 1054
- 2001b, *ApJ*, 551, 921
- Steiner, A. W., Lattimer, J. M., & Brown, E. F. 2013, *ApJ*, 765, L5
- Tomsick, J. A., Gelino, D. M., Halpern, J. P., & Kaaret, P. 2004, *ApJ*, 610, 933
- van Kerkwijk, M. H., Breton, R. P., & Kulkarni, S. R. 2011, *ApJ*, 728, 95
- Webb, N. A. & Barret, D. 2007, *ApJ*, 671, 727
- Wijnands, R., Heinke, C. O., & Grindlay, J. E. 2002, *ApJ*, 572, 1002
- Wiringa, R. B., Fiks, V., & Fabrocini, A. 1988, *Phys. Rev. C*, 38, 1010
- Zavlin, V. E., Pavlov, G. G., & Shibanov, Y. A. 1996, *A&A*, 315, 141

This 2-column preprint was prepared with the AAS L^AT_EX macros v5.2.